



# A rapid analytical assessment tool for three dimensional electrode microstructural networks with geometric sensitivity



George J. Nelson<sup>a,b,1</sup>, Arata Nakajo<sup>a,b</sup>, Brice N. Cassenti<sup>a,b</sup>, Matthew B. DeGostin<sup>a,b</sup>, Kyle R. Bagshaw<sup>a,b</sup>, Aldo A. Peracchio<sup>a,b</sup>, Guoliang Xiao<sup>a,c</sup>, Steve Wang<sup>d</sup>, Fanglin Chen<sup>a,c</sup>, Wilson K.S. Chiu<sup>a,b,\*</sup>

<sup>a</sup> HeteroFoam Center, a DOE Energy Frontier Research Center, United States

<sup>b</sup> Department of Mechanical Engineering, University of Connecticut, United States

<sup>c</sup> Department of Mechanical Engineering, University of South Carolina, United States

<sup>d</sup> Advanced Photon Source, Argonne National Laboratory, United States

## HIGHLIGHTS

- Analytical approach to assess 3-D electrode microstructural networks.
- Studied 3-D microstructures in  $\text{Sr}_2\text{Fe}_{1.5}\text{Mo}_{0.5}\text{O}_{6-\delta}$ , a redox stable SOFC electrode.
- Significant reduction in memory requirements and computational time was observed.
- Predictions validated to experimental measurements and detailed 3-D finite element simulations.

## ARTICLE INFO

### Article history:

Received 20 March 2013

Received in revised form

1 July 2013

Accepted 2 July 2013

Available online 12 July 2013

### Keywords:

Microstructure

Fuel cell

Design

Electrode

Electrochemical fin

Segmentation

## ABSTRACT

Electrochemical fin theory is applied to the microstructural analysis of  $\text{Sr}_2\text{Fe}_{1.5}\text{Mo}_{0.5}\text{O}_{6-\delta}$  (SFM), a redox stable solid oxide fuel cell (SOFC) electrode. The electrode microstructure is imaged by X-ray nanotomography, then partitioned into a network of resistive components with distinct geometric characteristics. The network is analyzed using an analytical electrochemical fin network model. The resulting predictions of electrode performance are compared to predictions made using three-dimensional finite element simulations of charge transport with surface electrochemical reactions in the imaged microstructure. For a representative subvolume of the structure, the electrochemical fin and finite element models provide comparable predictions. Analysis of larger representative volume elements extracted from the X-ray nanotomography data demonstrates good agreement with experimental measurements of the electrodes analyzed. Finally, advantages of applying the analytical electrochemical fin network models to real microstructures are addressed, particularly with respect to significant reduction in memory requirements and computational time. The use of the electrochemical fin theory is able to rapidly analyze real microstructures with microstructural details that are comparable to finite element and lattice Boltzmann methods, but at volume sizes that finite element and lattice Boltzmann methods were not able to perform due to limits in memory and computational time.

© 2013 Elsevier B.V. All rights reserved.

## 1. Introduction

Electrochemical energy storage and conversion devices, including fuel cells and batteries, are promising means for

\* Corresponding author. Department of Mechanical Engineering, University of Connecticut, United States.

E-mail address: [wchiu@engr.uconn.edu](mailto:wchiu@engr.uconn.edu) (W.K.S. Chiu).

<sup>1</sup> Current affiliation: Department of Mechanical and Aerospace Engineering, University of Alabama in Huntsville, United States.

managing diverse and variable energy resources to meet continually growing societal energy demands. These devices rely upon distinct arrangements of chemically active materials and phases supporting transport of reactants and charge. Such material systems are classified as heterogeneous functional materials, or HeteroFoams [1,2]. Furthering the state-of-the-art for electrochemical energy storage and conversion devices requires directed design of these materials at the micron and nanometer scale to create more effective reaction sites and supply reactant species to these sites in a more efficient manner. Within the realm of solid oxide fuel cells

Nomenclature			
$A_b$	cross-sectional area at the fin structure network base, $m^2$	$R_{pol}$	area specific polarization resistance, $\Omega m^2$
$A_c$	local fin cross-sectional area, $m^2$	SQ	sintering quality
$A_{c,b}$	cross-sectional area at the fin base, $m^2$	$T$	temperature, K
$A_f$	total fin surface area, $m^2$	$V$	voltage, V
$A_s$	local fin surface area, $m^2$	<i>Greek</i>	
$F$	Faraday constant, $C mol^{-1}$	$\varepsilon_f$	fin effectiveness
$i_{tot}$	total current, A	$\eta_f$	fin efficiency
$i_0$	exchange current density, $A m^{-2}$	$\rho_{ct}$	charge transfer resistivity, $\Omega m$
$L$	length of fin segment, m	$\rho_{io}$	ionic resistivity, $\Omega m$
$R$	ideal gas constant, $J mol^{-1} K^{-1}$	$\sigma_{io}$	ionic conductivity, $S m^{-1}$
$R_{ct}$	area specific charge transfer resistance, $\Omega m^2$	$\varphi$	potential difference, V
		$\varphi_b$	potential difference at the fin base, V

(SOFCs) a host of methods have emerged to tailor electrode microstructural morphology as a means of improving cell performance [3–5]. The advent of these capabilities has given rise to an analytical electrochemical fin modeling concept: a method that permits rapid and accurate analysis of electrode designs using a set of microstructural components with distinct geometries [6,7]. While emerging SOFC fabrication techniques permit an increasing level of deterministic control over microstructural geometry, the resulting structures are not as clearly defined as the controlled structures suggested by electrochemical fin and other microstructural models. Furthermore, established electrode production techniques result in complex microstructures with highly varied geometric characteristics. The capability to incorporate complex microstructural morphology into analytical models could benefit from continued microstructural design efforts.

X-ray nanotomography and focused ion beam-scanning electron microscopy (FIB–SEM) now permit observation and characterization of complex, three-dimensional SOFC microstructure with elemental [8–10] and chemical sensitivity [11]. Drawing on the available digitized microstructural data, a nexus has formed between these three-dimensional imaging methods and advanced transport modeling techniques such as the lattice Boltzmann method (LBM) and finite element method. Grew et al. [8] used phase-specific microstructural data obtained through absorption contrast imaging and X-ray nanotomography as a geometric domain for LBM models of gas and charge transport in SOFC Ni–yttria stabilized zirconia (YSZ) anodes. Subsequent mapping of ohmic losses back onto the microstructural dataset enabled quantification of microstructure induced resistive losses and the related identification of potentially problematic regions within the SOFC anode. Using microstructural data obtained with FIB–SEM serial sectioning, Shikazono et al. [12] and Matsuzaki et al. [13] employed LBM to determine the local electrochemical potential distributions for oxygen ions and electrons in SOFC composite anodes and mixed ionic electronic conducting (MIEC) cathodes, respectively. Microstructural data obtained from X-ray nanotomography measurements has also been applied as the geometric domain in anode gas transport models solved via finite element calculations [14]. Such applications of computing power are promising, but implementation of these techniques on larger regions of the heterogeneous electrode microstructure requires either significantly increased computational cost or the application of numerical schemes that trade accuracy for gains in solution speed while still requiring implementation on limited volume sizes [13].

Percolation theory [15–19] and resistor network models [20–24] of SOFC electrodes provide one pathway for faster analysis while retaining microstructural information. Costamagna et al. [15] developed a model for microstructural charge transport based

upon the analytical solution of an ordinary differential equation comparable to the equation governing the behavior of constant cross-section thermal fins. Overpotential distributions within composite anodes were used to determine polarization resistances. The use of effective conductivities based on percolation theory allowed for exploration of anode performance optima with respect to percolation thresholds. This work was later expanded by Canarozzo et al. [16] using a numerical model that included the effects of mass transfer in the pore phase based on the dusty-gas model for gas transport. Similar distributed charge transfer behavior was analyzed for a full anode-supported SOFC by Zhu and Kee [17], who demonstrated trade-offs between mass and charge transport associated with a range of particle sizes.

Further discretization of the microstructure can be achieved by implementing numerical solutions of resistive networks [18,20–22]. Sunde [22–24] used resistive network models to analyze composition dependent conductivity and polarization resistance in composite SOFC electrodes. Schneider et al. [20,21] addressed the effects of fabrication through the use of direct numerical sintering simulations coupled to the solution of the resulting resistor network, yet the structures assessed are initialized from a packing of consistently sized spherical particles. A common thread among these analyses is that they typically operate in terms of average (effective) properties such as spherical particle sizes. While particle sizes of individual phases may vary, specific size and 3-D microstructural variations within a given phase are not necessarily considered.

Models based upon an extended surface electrode concept provide a third approach to the analysis of electrode transport and the assessment of SOFC performance. Kenjo et al. [25,26] first presented a similar approach by applying thin film electrolyte models, commonly used for battery modeling, toward SOFC electrode analysis. Tanner et al. [27] later adapted this model to an extended surface visualization by treating the electrolyte as an extended surface coated with electrocatalyst particles. As with related percolation and resistor network models, these works provided insight into the relation between bulk electrode geometry, microstructure, and SOFC performance. However, the details of microstructural geometry beyond porosity effects were not explicitly assessed. The capability to include further details of the electrode solid phase geometry has been developed by Nelson et al. [6,7]. Drawing upon an analogy to heat transfer from extended surfaces, this analytical electrochemical fin model provides a tool for rapidly assessing the quality of electrode microstructures. By using analytical solutions to equations describing charge transport in variable cross-section structures, this approach is capable of capturing the effects of interparticle contact geometry and other detailed 3-D microstructural features that result from electrode

fabrication. While useful, this model would benefit from extending the set of geometries used to describe electrodes beyond composites of well controlled geometric entities. Such an extension can readily connect with three-dimensional imaging techniques and lead to a better understanding of the performance impacts of real SOFC electrode microstructures.

In this paper, the electrochemical fin modeling concept is adapted to study networks of resistive components with distinct geometric characteristics. The general concept of this adaptation is illustrated in Fig. 1a. A real microstructure, obtained via three-dimensional imaging, is separated into individual network segments. These segments are subsequently characterized to determine appropriate parameters for use in charge transport analyses. Modeling of charge transport in this adaptation is based on the dimensionless form of the electrochemical fin approach previously introduced by the authors [6]. The resulting modeling approach is applied toward the analysis of real, 3-D SOFC electrode microstructures imaged using X-ray nanotomography. Methods are presented for partitioning the segmented three-dimensional microstructural data into individual resistive components and subsequently calculating the appropriate dimensionless model parameters. SOFC electrode microstructures are analyzed using this network-based analytical model, and comparisons are made to more detailed finite element analysis (FEA) simulations and experimental predictions of polarization resistance [28,29]. The

benefits of implementing the network form of the electrochemical fin theory to real microstructures are discussed. Most notably, these benefits include marked reduction in memory requirements and computational time.

## 2. Methodology

### 2.1. Analytical electrochemical fin model

The quality of an electrode microstructure can be rapidly assessed using the electrochemical fin theory previously defined by the authors [6,7]. In this approach the electrode microstructure is abstracted as an extended surface of charge conducting material, as shown in Fig. 1b. Conduction within this material is treated as ohmic and one-dimensional along the path of the underlying network structure, with no space charge effects considered [7]. A portion of the charge passing through the solid structure is consumed at the surface by a charge transfer reaction that is described by linear charge transfer kinetics. Similar heuristics have been applied in the analysis of SOFC electrodes using both extended surface approaches and percolation theory [15,16,22–27]. However, the resulting models generally treat transport using a governing equation that tacitly assumes a constant cross-sectional area is available for conduction. Additional influence of the electrode microstructure can be captured by allowing cross-sectional area to vary over the extend surface. This modification produces an electrochemical fin model that is based on the analytical solution of a one-dimensional governing ordinary differential equation, Eqn. (1), that describes the electrode overpotential distribution. This modeling approach has been found to sufficiently capture the experimentally observed behavior of SOFC electrodes, including the capability to account for the effects of sintering on transport within electrode microstructures [6].

$$\frac{d^2\varphi}{dx^2} + \frac{1}{A_c} \frac{dA_c}{dx} \frac{d\varphi}{dx} - \frac{1}{\sigma_{io}R_{ct}A_c} \frac{dA_s}{dx} \varphi = 0 \quad (1)$$

$$\varphi = V - V_{ref} \quad (2)$$

As noted above, the formulation of Eqn. (1) relies upon several simplifying assumptions requiring further justification. The assumption of one-dimensional ohmic conduction in the solid phase is of greatest importance among these assumptions. Charge transport can be significantly affected by the presence of space charge regions at small interparticle contact regions [3,30]. Furthermore, small contact interparticle contact regions that result from incomplete sintering of the electrode will constrict the current flowing through the electrode, giving rise to multi-dimensional transport. Comparing analytical electrochemical fin analyses to more detailed finite element models that account for the effects of space charge regions and multi-dimensional transport has demonstrated that the simplified approach presented can provide performance assessments that are sufficient for rapidly screening potential electrode microstructures [7]. Specifically, electrode configurations that are deemed to have poor performance using the electrochemical fin model show comparable or poorer performance when analyzed using more detailed finite element models. The largest deviation is observed for microstructures with small interparticle contacts and materials that generate space charge regions that are large relative to particle size.

A key benefit of the analytical approach discussed above is that it sheds light on dimensionless parameters and performance metrics that can be used to describe the morphology and performance of SOFC electrode microstructures. The interplay between microstructural morphology, material properties, and operating

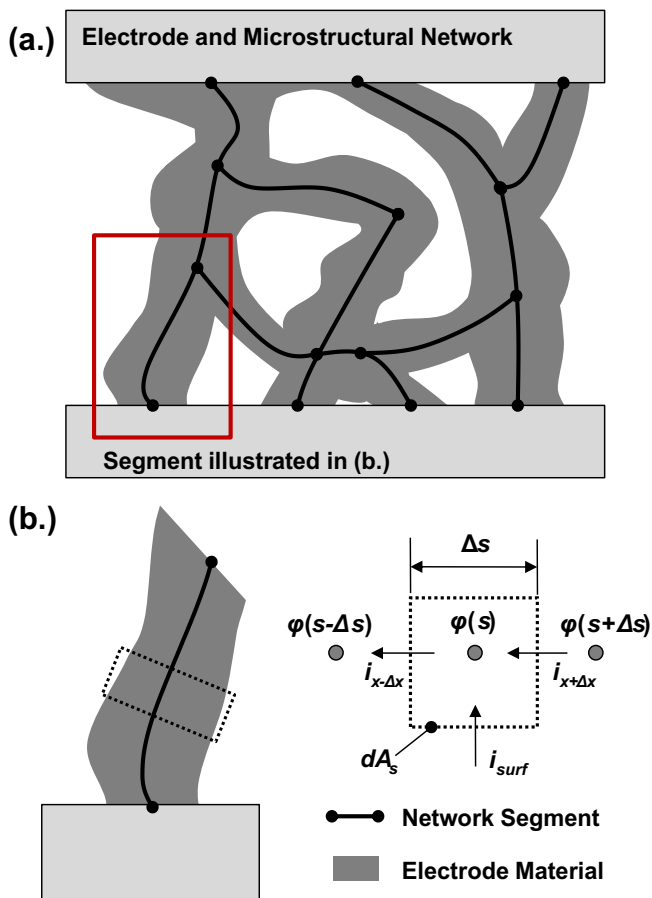


**Fig. 1.** (a) Using digital image processing tools the solid phase microstructure of an SOFC electrode can be separated into an underlying network. (b) Individual segments comprising this network can be characterized to determine parameters for use in an electrochemical fin charge transport model. In this model, potential distributions along the network segments are assessed based on analytical solutions to a one-dimensional ordinary differential equation developed from a charge balance on a differential volume.

conditions can be described by defining a set of basic dimensionless parameters: a dimensionless length ( $x^* = x/L$ ), a dimensionless potential ( $\varphi^* = \varphi/\varphi_b$ ), and two dimensionless areas ( $A_c^* = A_c/A_{c,b}$  and  $A_s^* = A_s/A_{c,b}$ ). Based on these parameters Eqn. (1) can be cast in a dimensionless form, Eqn. (3).

$$\frac{d^2\varphi^*}{dx^{*2}} + \frac{1}{A_c^*} \frac{dA_c^*}{dx^*} \frac{d\varphi^*}{dx^*} - \frac{L}{\sigma_{io}R_{ct}A_c^*} \frac{dA_s^*}{dx^*} \varphi^* = 0 \quad (3)$$

Inspection of Eqn. (3) yields two additional dimensionless parameters that can be used to describe electrode morphology and charge transfer characteristics. The first of the parameters is a resistivity ratio, Eqn. (4), which quantifies the magnitude of resistance to conductive transport relative to the resistance to surface charge transfer. This parameter can be recognized as the coefficient of the last term on the left hand side of Eqn. (3). A second parameter, a sintering quality, can be derived from the coefficient of the second term on the left hand side of Eqn. (3). The sintering quality, expressed in Eqn. (5), quantifies the degree of variation in the cross-sectional area that occurs along the length of an electrode. A low sintering quality would correspond to microstructures with small necks between particles, which serve to increase ohmic resistance. The use of these parameters to describe real SOFC microstructures is enabled by integrating the expressions in Eqns. (4) and (5) over discrete regions partitioned from microstructural image data. A similar approach has been applied for deterministic structures [6]. Details of this procedure will be discussed in a later section.

$$\frac{\rho_{io}}{\rho_{ct}} = \frac{L^2}{\sigma_{io}R_{ct}} \frac{1}{A_c} \frac{dA_s}{dx} \quad (4)$$

$$SQ = \left[ \frac{L}{A_c} \frac{dA_c}{dx} \right]^{-1} \quad (5)$$

In addition to the parameters defining electrode morphology and properties, a set of dimensionless metrics has been developed to describe electrode performance. Drawing upon the analogy between charge transport in SOFC electrodes and thermal fin behavior, an efficiency may be defined according to Eqn. (6). This efficiency quantifies the ohmic losses incurred within the electrode by comparing the total charge transferred by the electrode to the charge transfer that would be realized in the absence of ohmic losses. Similarly, an effectiveness can be defined for an extended surface electrode according to Eqn. (7). The effectiveness quantifies charge transfer gains made by the use of a complex extended surface electrode by comparing the charge transferred by the extended surface electrode to the charge that would be transferred by an unmodified surface. The effectiveness can be related to the electrode polarization resistance using Eqn. (8), where the charge transfer resistance is defined based on the exchange current density, as shown in Eqn. (9). In the present work, we focus on the polarization resistance as a predictor of electrode performance. The primary reason for this focus is that the polarization resistance provides a means of making preliminary comparisons to experimental results.

$$\eta_f = \frac{i_{tot}}{(1/R_{ct})A_f\varphi_b} \quad (6)$$

$$\varepsilon_f = \frac{i_{tot}}{(1/R_{ct})A_b\varphi_b} \quad (7)$$

$$R_{pol} = \frac{R_{ct}}{\varepsilon_f} \quad (8)$$

$$R_{ct} = \frac{i_0F}{RT} \quad (9)$$

The dimensionless parameters and metrics outlined above have been used to analyze microstructures based on predefined shapes [6,7]. However, as will be demonstrated, the dimensionless model also allows complex electrode microstructures with more arbitrary shapes to be approximated with a smoothed exponential profile. The definition of this profile as exponential follows from the separation and integration of Eqns. (4) and (5), assuming a fixed sintering quality and a fixed resistivity ratio for the portion of the microstructure that is analyzed. Electrode performance assessment is achieved by casting Eqn. (3) in terms of the constant sintering quality and constant resistivity ratio, Eqn. (10), and subsequently solving the resulting ordinary differential equation. This solution, in general form, is given in Eqns. (11) and (12).

$$\frac{d^2\varphi^*}{dx^{*2}} + \frac{1}{SQ} \frac{d\varphi^*}{dx^*} - \frac{\rho_{io}}{\rho_{ct}} \varphi^* = 0 \quad (10)$$

$$\varphi^*(x^*) = C_1 \exp(\alpha_1 x^*) + C_2 \exp(\alpha_2 x^*) \quad (11)$$

$$\alpha_{1,2} = \frac{1}{2} \left[ -\frac{1}{SQ} \pm \sqrt{\frac{1}{SQ^2} + 4\left(\frac{\rho_{io}}{\rho_{ct}}\right)} \right] \quad (12)$$

The general solution outlined in Eqns. (11) and (12) permits extension of the electrochemical fin concept to microstructural networks observed within real SOFC electrodes. This extension starts by parsing the microstructure into segments using image processing techniques. These techniques, described further in Section 2.3, include: 1) filtering and segmentation of phases to generate a digitized representative volume element (RVE), 2) skeletonization of the RVE to reveal microstructural networks, 3) edge-based partitioning of the structure into individual network segments, and 4) geometric analysis of the resulting network segments.

Asserting that individual segments within a given microstructural geometry are governed by the general solutions presented above, the network can be analyzed. For a microstructure composed of multiple segments the set of general solutions are constrained at vertices connecting segments and network boundaries based on equipotential and current conservation conditions. The resulting system of equations can then be solved to predict electrode performance. This arrangement effectively defines and analyzes a circuit of ohmic and charge transfer resistances that is sensitive to localized microstructural characteristics. While this sensitivity does not extend to detailed variations along an individual segment within the microstructure, it provides sufficient approximation of the microstructure at a finer level of detail than bulk homogenization and enables rapid performance assessment.

## 2.2. X-ray nanotomography measurements

In the present work real SOFC electrode microstructures are analyzed using electrochemical fin theory. The microstructural data analyzed are taken from porous SOFC electrodes measured using X-ray nanotomography. This data originates from samples of the mixed conducting perovskite  $Sr_2Fe_{1.5}Mo_{0.5}O_{6-\delta}$  (SFM). This material has proven stable in both oxidizing and reducing environments and is therefore considered applicable for use in cathodes or anodes



[31]. The SFM electrodes assessed in the present work are porous electrodes extracted from a symmetric cell and contain a single solid phase. Further details of the fabrication and electrochemical characterization of these symmetric cells have been outlined by Liu et al. [31]. Cylindrical core samples approximately 10  $\mu\text{m}$  in diameter and 15–20  $\mu\text{m}$  in height were extracted from these symmetric cells using an FEI Strata focused ion beam-scanning electron microscope. The use of such samples with a consistent X-ray absorption cross-section has been found to improve image quality, which greatly facilitates reconstruction and segmentation [32,33]. The SFM samples were imaged using the transmission X-ray microscope (TXM) facilities at APS beamline 32-ID-C. X-ray nanotomography measurements for each sample consisted of a series of 181 transmission images taken over a rotational range of  $\pm 90^\circ$ . 181 transmission images were found to be adequate for the feature sizes of interest in the SFM samples, which were well above the spatial resolution of the microscope. In addition, it mitigated the issues of image alignment and experimental runtime associated with collecting image data at a very large number of angles. Since only a single solid phase is present in the SFM, nanotomography measurements were performed at a single X-ray energy level, 8 keV. The transmission image data was then reconstructed using a filtered back projection algorithm to generate a three-dimensional dataset, or tomogram. A cross-sectional slice taken from the reconstructed X-ray nanotomography dataset, Fig. 2a, demonstrates that imaging at a single X-ray energy level proved sufficient to distinguish the solid SFM phase from the pore regions.

### 2.3. Image processing and microstructural characterization

The three-dimensional X-ray nanotomography data for the SFM samples was initially processed using the ImageJ software [34] to generate digitized representative volume elements (RVEs) for later analysis. Two representative volume elements (RVEs) of 200 pixels (5  $\mu\text{m}$ ) to a side and a cylindrical sample volume with a diameter of

9  $\mu\text{m}$  and a height of 11.25  $\mu\text{m}$  were sectioned from the data. Minor filtering was performed by first applying a Gaussian blur filter to reduce pixilation and remove outliers, which can both stem from the image acquisition process itself or from imperfect alignment during the reconstruction process. Next, a sharpening filter was applied to ensure contrast was maintained at solid-pore boundaries. The sharpening filter was followed by repetition of the Gaussian blur, and a subsequent mean shift to smooth gray values within each phase. After filtering, rather homogeneous grayscale values within each phase and significant contrast between the two phases permitted the discrete labeling of the structure by a simple gray-scale thresholding method. An example of a final thresholded region of interest within the SFM sample is shown in Fig. 2b.

Application of the analytical electrochemical fin modeling framework to a real structure requires retrieving topological and morphological information from an RVE. In the present approach, skeletonization of the 3-D SFM nanotomography data provides a representation of the structure as a set of vertices connected by edges. This skeletonization step provides a basis for further partitioning of the SFM phase into a network of segments of different shapes for morphological characterization. The characterization tool consists of Matlab (Mathworks, Natick, MA) routines that call Avizo (Visualization Science Group, Burlington, MA) scripts for specific procedures. The general workflow is summarized by Fig. 2 and described hereafter. It should be noted that for the current analyses, only regions that connect opposite RVE faces are considered. This contiguity is determined using a labeling procedure. A digitized representative volume element, Fig. 2c, is produced from the thresholded region of interest and passed through a series of calculations. These calculations are referred to as skeletonization, edge-based partitioning, and analysis of individual segments.

#### 2.3.1. Skeletonization

To begin the skeletonization portion of the image processing workflow (Fig. 2c) closed pores within the solid phase are filled to

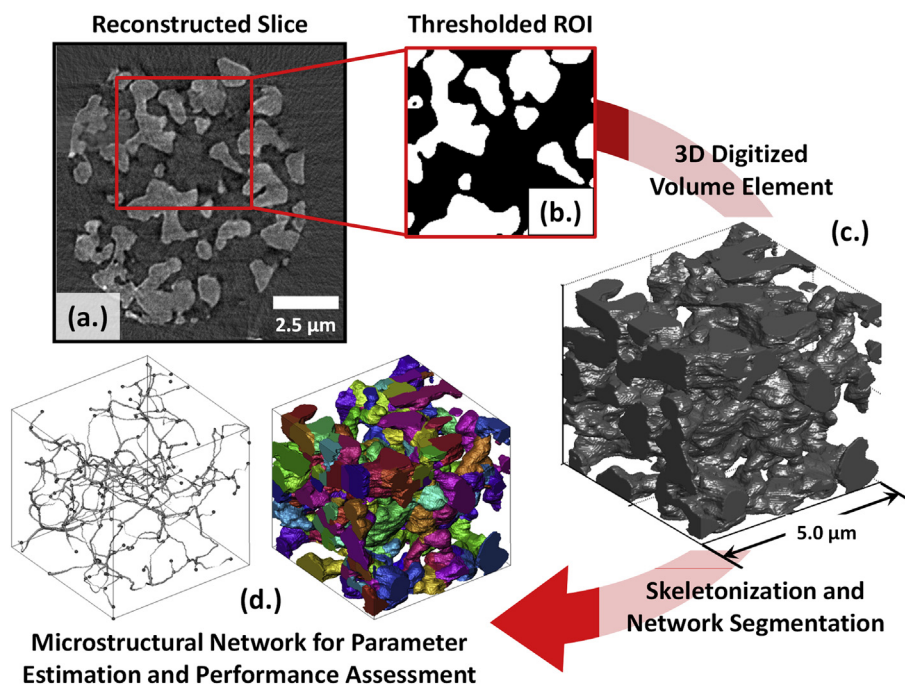


**Fig. 2.** General process workflow for generating an electrochemical fin network from a real SOFC electrode microstructure: (a) X-ray nanotomography data is reconstructed to generate a grayscale tomogram; (b) a region of interest (ROI) within the grayscale image data is thresholded to produce a digitized volume element representing the distinct phases of the electrode; (c) the digitized data is passed to a skeletonization algorithm and an initial microstructural skeleton is further partitioned into a network; (d) the particles comprising the network are characterized to yield electrochemical fin morphological parameters and the network performance is subsequently assessed (color online).

prevent the generation of excessive edges around them and consequent unrealistic partitioning of the solid phase volume. The distance map of the filled phase is computed assuming symmetry at the sample boundaries. This assumption ensures that vertices (or edge points) are generated at sample boundaries, which facilitates the imposition of model boundary conditions. The skeleton is then extracted by thinning the distance map using the algorithm from Sato et al. [35], which is implemented in Avizo. This extraction serves as a starting point from which the vertices, list of edges, and segment connectivity information are modified and updated to ensure the SFM solid phase is consistently represented. Adjustment of the microstructural network description is conducted subject to the following four rules:

1. Classification of the edges is performed depending on their length, location and connectivity. Edges with connectivity of 0 at a given vertex are labeled as dead-ends.
2. Edges that touch but do not yield a vertex on the boundaries of the RVE subjected to the network boundary conditions are split at the vertex where the local thickness provided by the distance map is the smallest.
3. Edges below a specified length that are connected to other edges at their two vertices, hereafter referred to as connecting edges, are removed from the skeleton and treated as connecting clusters, practically equivalent to a single vertex. For the microstructure studied here, tests showed that a minimum value of 6 voxels (0.15  $\mu\text{m}$ ) produced consistent results and reduced errors in the subsequent partitioning procedure.
4. Dead-end edges smaller than a specified minimum length are recorded for deletion after the initial partitioning of the SFM structure. In the present studies a minimum length of 17 voxels (0.425  $\mu\text{m}$ ) produced consistent results and reduced errors in the subsequent partitioning procedure.

### 2.3.2. Edge-based partitioning

Following the modification of the skeleton data an edge-based partitioning step is performed to determine the final network (Fig. 2d). The analytical modeling approach described in Section 2.1 requires that the network is made of segments with two contact zones only. Therefore, our partitioning approach is taken with the intent of identifying segments that serve as transport channels within the network, rather than the starting particles used to produce the structure. The segments are identified by partitioning the SFM phases using a watershed algorithm implemented in Avizo. The skeleton edges are used as markers, as opposed to the local maxima of the distance map. This approach is more complicated and requires increased attention during the generation of the markers that drive the watershed algorithm, because partitioning is not realized at the necks. The markers are generated by dilation of the labeled skeleton edges, excluding the vertices and clusters. Dilation by 2–3 voxels is typically sufficient to ensure that each label is not fragmented. The boundaries between the labels are then detected using an edge-detection Sobel filter and removed by thresholding. The procedure is performed separately for connecting and dead-end edges. The markers generated from the latter are added afterward to favor the integrity of the connecting edges over that of the dead-end edges.

The partitioned volume is then searched for small segments that do not connect to the pore phase and are therefore merged within the solid volume. These are reclassified as clusters and the watershed partitioning is applied to the filled solid volume using the updated list of markers. The procedure is repeated until no such particles remain. The coherent correspondence between edges and segments is verified and the particles are labeled accordingly.

Undesirable segments that do not relate to a marker may be generated when applying watershed partitioning to a complex structure. These are merged with their dominant neighbor segment that is identified by analyzing the inter-segment interfacial surfaces. A similar merger step is performed on dead-end edges that are removed according to rule four listed above. Tests showed that this sequence provides a better control of the partitioning than the initial removal of all the dead-end edges that are shorter than the minimum length. A final partitioned volume and its related network are shown in Fig. 2d.

### 2.3.3. Analysis of individual segments

The partitioning of the SFM solid phase described previously enables retrieval of a segment's morphological and topological information needed by the analytical modeling approach described in Section 2.1. Averaged values of the sintering quality SQ and resistivity ratio  $\rho_{\text{io}}/\rho_{\text{ct}}$  are computed for each segment within the network structure, to comply with Eqns. (10) and (11). For the sintering quality term, this requirement limits the profiles that can be rigorously treated to exponential variations of the cross-section and reduces the needed measurements to that of the intra-phase interfacial surface areas  $A_1$  and  $A_2$ :

$$\text{SQ} = \left[ \int \frac{1}{A_c} \frac{dA_c}{dx} dx \right]^{-1} = \left[ \ln \frac{A_2}{A_1} \right]^{-1} \quad (13)$$

Sub-partitioning is applied to mitigate this limitation by providing sensitivity to one constriction per segment. The methodology proposed hereafter will be refined in the future for a comprehensive treatment of constrictions within the segments. Vertex-based partitioning of the structure is first carried out following a similar approach to that applied for edge-based partitioning. Then, the skeleton points that intersect the watershed boundaries are identified and the computed cross-section at this coordinate is used for sub-partitioning of the segment. The intersection between the segment and the plane normal to the skeleton point may be comprised of unconnected cross-sections, which may yield an incorrect determination of the intra-phase interfacial surface area at the sub-partitioning point. This possibility is overcome by applying a labeling procedure to the detected cross-section areas to identify the relevant area for transport analysis, i.e., the one that contains the edge point. The skeleton topology and the labeling of the partitioned solid phase (SFM) are then updated. The actual inter-segment interfacial surface contact areas at the main skeleton vertices are measured on the isosurface extracted from the digitized sample volume labeled for each segment, using the marching cube algorithm implemented in Avizo. Because of the complexity of real material microstructures, discrepancies between actual physical inter-segment contacts and those listed in the skeleton cannot be avoided. The physical contacts that are detected for each particle are tentatively grouped into two zones, corresponding to the two main edge vertices, by detecting the mesh vertices common to several contact surfaces.

Once the structure is sub-partitioned, the length  $L$  of each segment is measured after smoothing of the skeleton coordinate points to avoid overestimation. The volume and total surface area  $A_s$  of each segment is then extracted to compute the resistivity ratio according to Eqn. (14). Here, the geometric factor in parentheses is approximated using the measured surface area to volume ratio. This approximation introduces some error in the geometric factor. However, when examined for conical geometries, maximum cross-sectional area to minimum cross-sectional area ratios of up to 3:1 demonstrated errors of less than 5%. For the structures examined in the present work these ratio are on average less than 3:1.

$$\frac{\rho_{io}}{\rho_{ct}} = \frac{L^2}{\sigma_{io} R_{ct}} \left( \frac{1}{L} \int_0^L \frac{1}{A_c} \frac{dA_s}{dx} dx \right) \approx \frac{L^2}{\sigma_{io} R_{ct}} \frac{A_s}{V} \quad (14)$$

#### 2.4. Finite element model

To better determine the benefits and shortcomings of the analytical electrochemical fin approach charge transport within the SFM microstructure was analyzed using a three-dimensional finite element model. Initial development of the network partitioning approach was performed on a small volume,  $100 \times 100 \times 110$  voxel, of the SFM microstructure. This same three-dimensional structure was applied as the computational domain in the finite element studies. The general geometry of this volume may be seen in the results presented in Fig. 3a and b. This small structure was chosen to facilitate direct comparison of model predictions, particularly with respect to analyzing detailed potential distributions. As demonstrated by Lynch et al. [36] successful meshing and analysis of such complex domains may be achieved using the open source software Iso2Mesh in conjunction with the COMSOL Multiphysics 4.2 finite element analysis (FEA) software.

In the present work, meshing of the volume was completed using Iso2Mesh [37], which is used to generate a tetrahedral mesh from an isosurface defined based on the binary nanotomography volume data. To generate an accurate representation of the microstructure mesh parameters were specified to control the

allowable deviation from the initial isosurface. The maximum sphere radius for Delaunay triangulation was used to generate the surface mesh. The Delaunay triangulation process divides a given region into a set of triangles such that the minimum angle of each triangle is maximized. Details of the mathematics of this process are thoroughly discussed by Okabe et al. [38]. The first of these parameters allows for adjustment of the isosurface, a level set function between 0 and 1 describing the binary tomography data, within a given tolerance. The initial isosurface was generated for a level set at 0.5, and a tolerance of  $\pm 0.2$  was permitted. The second of these parameters controls the density of the surface mesh while preserving surface element quality. The maximum Delaunay radius was set at two pixels. Finally, a maximum element volume of three voxels was found to balance overall element count while retaining an accurate representation of the microstructure when compared to the initial isosurface representation. Node and element data from the mesh were converted to a NASTRAN file format and subsequently imported into COMSOL for analysis. The finite element model constructed addressed ohmic charge transfer within the solid phase. To permit a direct comparison of results, constant potential boundary conditions were applied at the surfaces representing the starting areas of constrained electrochemical fin vertices. A linear surface charge transfer boundary condition due to electrochemical reactions at the surface, similar to that applied in developing the analytical electrochemical fin model [6,7], was applied at the remaining surfaces within the computational volume. The final FEA models contained  $\sim 310,000$  quadratic

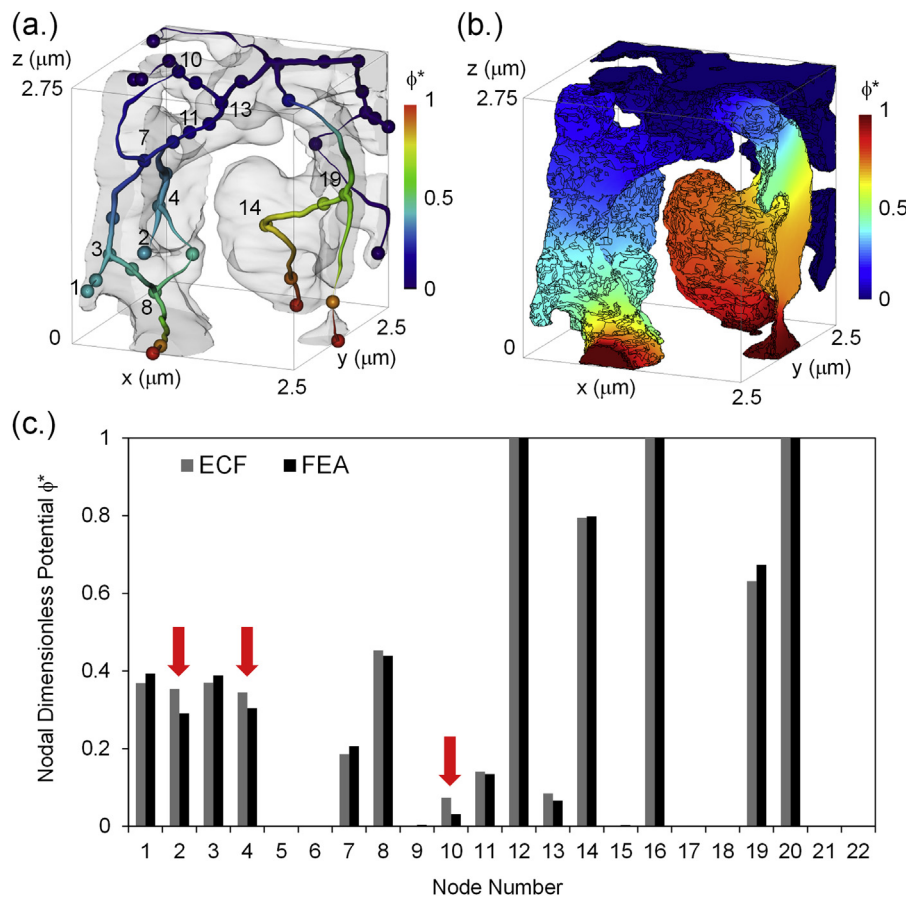


**Fig. 3.** Dimensionless potential distributions for a subvolume of the SFM microstructure predicted by the electrochemical fin (a) and finite element (b) models demonstrate reasonable agreement. (c) Point-to-point comparisons for the vertices defining the endpoints of segments within the microstructural network confirm this agreement, with the greatest discrepancies seen in regions with low potentials. The thickness of the segments in (a), which corresponds to the distance map value at the skeleton coordinate points, is provided for illustration purposes (color online).

tetrahedral elements with  $\sim 490,000$  degrees of freedom (DOF) for the  $100 \times 100 \times 110$  structure and 2–3 million quadratic tetrahedral elements with 3–4 million DOF for the  $200 \times 200 \times 200$  structures. For the  $200 \times 200 \times 200$  structures, FEA studies were run strictly to provide a measure of memory and computational time requirements.

### 3. Results

Using the electrochemical fin theory with microstructure representation, electrode performance can be rapidly predicted. However, determining the predictive capabilities of the electrochemical fin approach relative to more detailed modeling approaches is needed to better understand its benefits and limitations. A Dell Precision desktop workstation with 12 processors (dual six core Intel Xeon X5650, 2.66 GHz), 12 MB cache, 24 GB DDR3-1333 RAM, and an Intel 5520 chipset running Windows 7 Professional was used for the FEA and electrochemical fin analyses in this study. A side-by-side comparison of the dimensionless potential predicted for the electrochemical fin network and the dimensionless potential distribution predicted by the finite element model is shown in Fig. 3a and b. The color-coded points in Fig. 3a correspond to the skeleton points defined in the partitioning and network generation step of the image analysis. From inspection of these three-dimensional distributions, qualitative agreement between the two approaches can be seen. A more detailed comparison of the network model and finite element predictions of the potentials is given in Fig. 3c for the nodal locations defined by the endpoints of individual segments that compose the fin network. The finite element predictions are determined by interrogating the FEA solution at the fin network nodal locations, so a direct spatial comparison of the models is achieved. Locations where the discrepancy between the FEA and fin network predictions exceeds 5% of the base potential are noted with red arrows. The greatest disagreement, approximately  $\sim 8\%$ , is seen at vertex 2, which sits on a narrow protrusion located near the edge of the region examined. This error propagates to vertex 4, which shows the second highest error of  $\sim 6\%$ . An error of  $\sim 5\%$  is seen for vertex 10, also marked in Fig. 3c. This vertex is close to, but not located on, the zero potential boundary at the top of the computational domain shown. This discrepancy occurs because the transport path to these vertices through the fin network, i.e. between the errant vertices and the vertices where the boundary conditions are applied, is treated as being longer in the fin network than in the FEA model. If desired such errors could be corrected by applying boundary conditions to vertices within a specified distance of the edge of the domain. Comparison of potential drop across individual segments were also checked, but are not shown. The largest error seen in prediction of the potential drop was approximately 9% of the specified base potential, with only five segments showing an error greater than the 5% cut-off. Discrepancy at these levels is considered acceptable when comparing to the more detailed FEA model.

While point-to-point comparison provides a degree of confidence in the predictive capabilities of the electrochemical fin theory, it is important that predictions of microstructural performance metrics are also compared. To this end polarization resistance estimates from each model are compared in Table 1 to gauge the performance assessment capabilities of the fin approach in relation to the FEA model. As SFM is stable in reducing and oxidizing environments, it is capable of serving as a cathode and an anode in SOFC applications. Predictions made for cathode applications apply an exchange current density of  $0.18 \text{ A cm}^{-2}$ , while anode calculations apply an exchange current density of  $0.11 \text{ A cm}^{-2}$ . An oxide ionic conductivity of  $0.13 \text{ S cm}^{-1}$  is applied for the cathode, while an oxide ionic conductivity of  $0.0027 \text{ S cm}^{-1}$  was applied for the

**Table 1**

Electrochemical fin and finite element polarization resistance estimates for a  $100 \times 100 \times 110$  voxel volume extracted from the SFM X-ray nanotomography data.

Polarization resistance ( $\Omega \text{ cm}^2$ )		
Electrode	Electrochemical fin	FEA
Cathode	0.0027	0.0027
Anode	0.0489	0.0534

anode. It can be seen that predictions of the polarization resistance agree quite well for the cathode calculations. A larger discrepancy is seen on the anode side, which is more dominated by resistive losses due to the lower conductivity. In this case, the electrochemical fin network model estimates a lower polarization resistance. It should be noted that part of the discrepancy seen for the anode case may be related to a greater charge conservation error for the FEA case. On the cathode side, a charge balance error of 0.03% of the base current was achieved. For the anode side this error was between 1 and 2%. Significant charge balance errors were not seen for the electrochemical fin prediction in the cases reviewed. This is due to the fact that the analytical approach is inherently conservative, providing that areas at the segment endpoints are fixed according to appropriate constraints. Charge conservation is achieved because governing equations are derived directly from a current conservation relation [6] and the system of equations that is solved to determine the constants of integration for each segment, seen in Eqn. (11), is constructed by enforcing equipotential and charge conservation constraints within the structure. It should be noted that approximation of the irregular microstructure with an axisymmetric model may introduce errors in cases where conduction dominates transport, indicated by resistivity ratios well above 10. Such cases would correspond to low conductivities, low surface area to volume ratios, high charge transfer resistances, or a combination thereof. The individual network segments analyzed in this work have resistivity ratios well below unity. Thus the axisymmetric approximation of the microstructural segments is considered sufficient.

To test the predictive capabilities of the electrochemical fin approach on a broader scale, an assessment of the SFM electrode has been performed on a network partitioned from the  $200 \times 200 \times 200$  RVE, shown in Fig. 2c. The final network taken from this volume consisted of 513 individual segments after sub-partitioning, 273 segments prior to sub-partitioning. The separated particles and skeleton representation of this network are shown in Fig. 2d. Larger structures can be readily analyzed using the electrochemical fin approach, as will be discussed in later sections. However, the size of the X-ray nanotomography imaged sample limited extraction of larger volumes. A point cloud plot of the dimensionless potentials predicted within the  $200 \times 200 \times 200$  structure is shown in Fig. 4a, and the distribution of these potentials along the primary (z) transport direction is shown in Fig. 4b. For this portion of the microstructure, it can be seen that a majority of the potential drop occurs over the first couple microns of the network. Within the point cloud plot such regions can be seen clearly in the lower middle region of Fig. 4a. This data demonstrates that local potential distributions within the microstructure can be determined using the electrochemical fin model and detailed assessment of microstructural features can be performed.

If faster assessment of the microstructure is desired, an RVE averaged approach can be taken for representative regions of the sample. In this case, the methods used to determine the model parameters for individual segments within the network can be applied to the full representative volume element, without regard to partitioning of the more detailed microstructural network within the element. The surface area to volume ratio in this case is



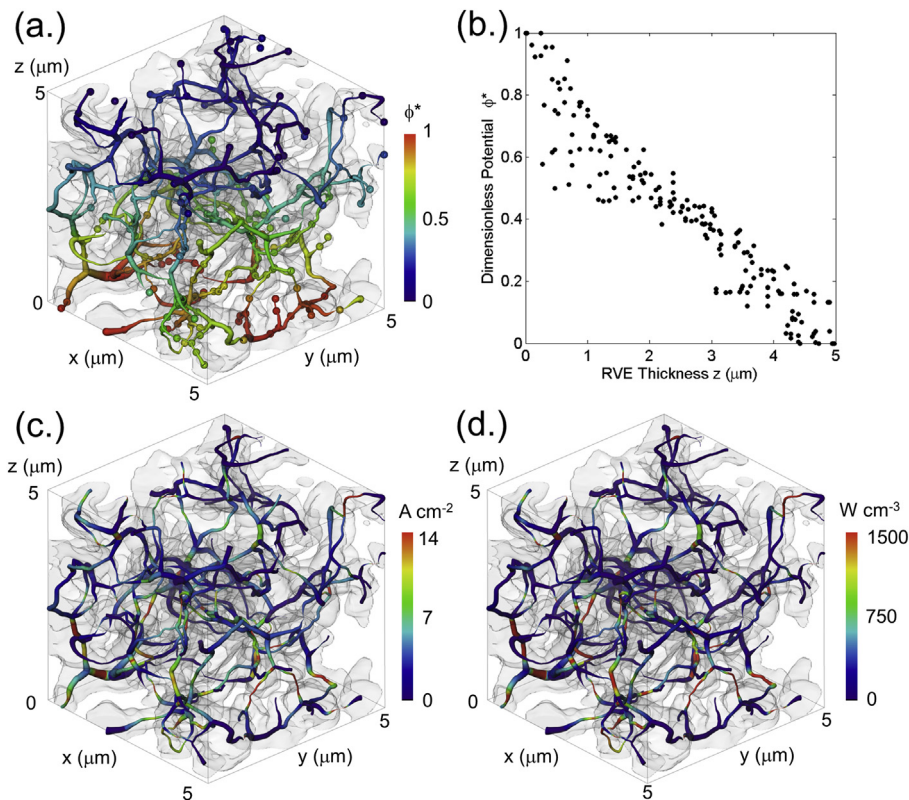


**Fig. 4.** The three-dimensional distribution of potential within a representative volume element (RVE) of the SFM microstructure (a) reveals regions of potential drop near constrictions within the microstructural networks. (b) Variations in the dimensionless potential predicted for the RVE network suggest additional network characteristics impact performance, particularly near the base of the structure ( $z = 0$ ). These characteristics impact local current density (c) and Joule heating (d) suggesting hot spots within the microstructure. Both of these quantities can be rapidly predicted using the electrochemical fin network model. The thickness of the segments in (a), (c), and (d), which corresponds to the distance map value at the skeleton coordinate points, is provided for illustration purposes (color online).

calculated for the entire RVE based on microstructural characterization routines described by Grew et al. [39,40]. The sintering quality is determined by applying Eqn. (13) to a given RVE in a predefined transport direction. This approach circumvents the labor-intensive network separation step, but sacrifices some accuracy in performance estimates as well as the capability to assess more localized transport. A similar lumped parameter approach was applied by Wilson et al. for analysis of FIB–SEM data taken from SOFC anodes [41,42]. A key distinction between their approach and the method applied in the current work is the application of the sintering quality term to account for variation in cross-sectional area for the volume analyzed. This RVE averaged approach does not account for the full impacts of microstructural geometry. These impacts can be classified as morphological, quantified by the sintering quality and surface area to volume ratio of the RVE or individual network segments, and topological, related to the arrangement of the segments comprising the network. Comparing the predictions of the network and RVE averaged approaches for this larger structure suggests that at a scale representing a full electrode topological characteristics of the microstructural network may exert a significant influence over the performance of the SFM electrodes studied.

In addition to the assessment of potential distributions, localized current density can be mapped within the structure. These local current densities can be used to determine localized Joule heating, or hot spots, based on the material resistivity. Distributions of the current density and localized Joule heating are shown in Fig. 4c and d for interior vertices in the fin network. For these distributions the voltage fixed at the base of the structure was set to yield a superficial current density of  $1 \text{ A cm}^{-2}$ . As verification of

these results, it is noted that the predicted heat generation rates are of similar magnitude as values predicted for YSZ structures using LBM transport simulations [40]. High local heat generation rates can be seen near constrictions in lower middle regions of the sample corresponding to large potential drops seen in Fig. 4a.

The overall performance of the electrode microstructure can be assessed based on the polarization resistance, which is commonly measured experimentally. Recent measurements of the polarization resistance of SFM electrodes have yielded values ranging from  $0.07 \text{ } \Omega \text{ cm}^2$  under cathodic operation [28,29] to  $0.27 \text{ } \Omega \text{ cm}^2$  under operation as an anode [31] at  $800^\circ \text{C}$ . Polarization resistance values predicted by the electrochemical fin model using ionic conductivities and exchange current densities associated with SFM applied as a cathode and an anode are shown as a function of RVE size in Fig. 5. The anode polarization resistance predicted by the electrochemical fin theory agrees with experimental measurements when a sufficient RVE size is considered. For the microstructure analyzed this agreement was seen for RVE sizes of  $\sim 3 \text{ } \mu\text{m}$  per side and higher. Experimental ranges shown are based on the work of Xiao et al. [28,29] and Liu et al. [31]. As noted, polarization resistances estimated by Wilson et al. [41,42] for composite electrode microstructures imaged with FIB/SEM showed similar disagreement with measured values depending upon the composition. So a degree of disagreement can be expected. A portion of this disagreement may be attributed to the exclusion of network topology in the averaged approach. For the cathodic case, analyses based on a fully partitioned network predict a higher polarization resistance of  $\sim 0.019 \text{ } \Omega \text{ cm}^2$  for the RVE of size  $5 \text{ } \mu\text{m}$  per side, suggesting that network effects may influence cathode performance predictions. Using parameters indicative of anodic operation, specifically a

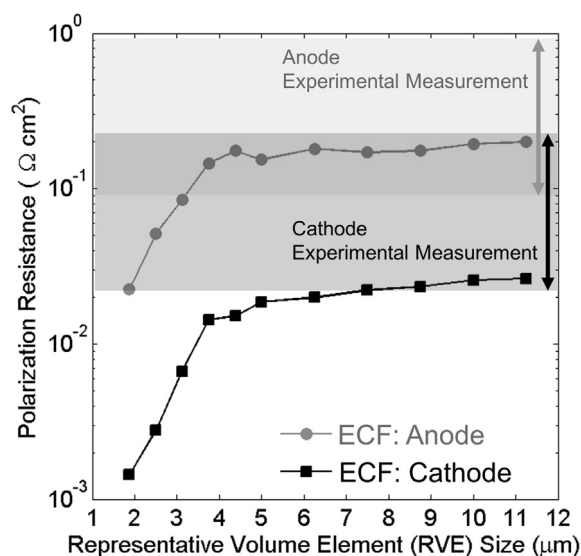


**Fig. 5.** Comparison of polarization resistance predicted by the analytical electrochemical fin model to experimental measurements for SFM electrodes at 800 °C [28–31]. The polarization resistances shown were calculated using the electrochemical fin network model.

conductivity of  $0.0027 \text{ S cm}^{-1}$  and an exchange current density of  $0.11 \text{ A cm}^{-2}$ , results in a predicted polarization resistance of  $\sim 0.15 \text{ } \Omega \text{ cm}^2$  for this same volume. The results for the anode lie within the range of experimentally observed polarization resistances. While the cathode values are close to the experimentally observed polarization resistance range, some disagreement is still seen. This additional discrepancy for the SFM material is likely due to the fact that effects associated with mixed conduction and space charge regions at interparticle contact points within the sintered structure are not accounted for in the electrochemical fin network model. It can be expected that these influences will be stronger within the cathode, where vacancy incorporation and the effects of varied oxygen partial pressure may exert greater influence. Nevertheless, the agreement of the analytical electrochemical fin model is within a reasonable range for providing a rapid assessment of the quality of the electrode microstructure, particularly considering computational costs associated with inclusion of these phenomena in an assessment of microstructural performance.

#### 4. Discussion

The merit of the electrochemical fin theory is that it provides a tool for the rapid assessment of tailored microstructures in electrochemical energy storage and conversion devices. This assessment capability will in turn aid continued microstructural design efforts. To confirm a gain in assessment capabilities, a comparison of computational performance is warranted. In Fig. 6 memory requirements are provided for the finite element model of the  $100 \times 100 \times 110$  structure, finite element models of two  $200 \times 200 \times 200$  RVEs taken from the nanotomography data, and the microstructural regions analyzed using the electrochemical fin theory, with polarization resistances given in Fig. 5. Computational times related to these cases are given in Table 2. For the electrochemical fin model cases the number of particles in the microstructural network partitioned from the RVE, using the skeletonization routine, is listed in the column labeled “Network Size”. These memory and time requirements account for only the solution of the systems of equations related to the numerical finite

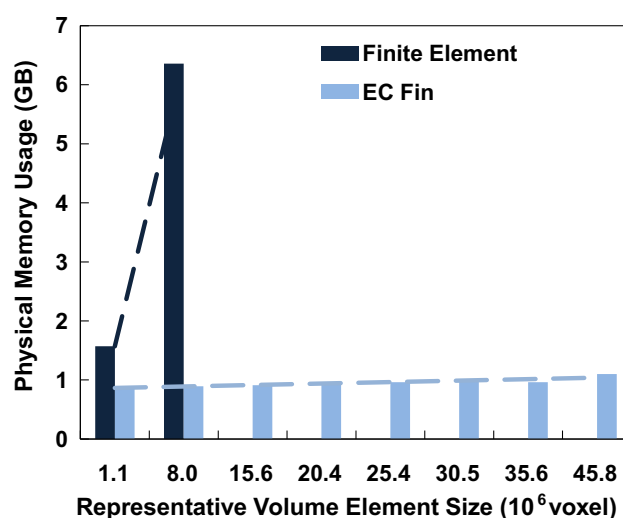


**Fig. 6.** Memory requirements for finite element calculations and electrochemical fin simulations of the SFM X-ray nanotomography microstructural data. Finite element analysis was not performed for the cases above  $8.0 \times 10^6$  voxel due to insufficient computational memory.

element and the analytical electrochemical fin network models. Both methods require the same basic segmentation of X-ray nanotomography data into solid and pore phases. The time required for meshing and skeletonization in the respective approaches are considered to be comparable, as both processes are automated but require review of the end result to ensure accurate solution.

The first benefit of the electrochemical fin approach lies in memory requirements. Taking advantage of the sparse matrix format, since it only solves for two constants  $C_1$  and  $C_2$  (shown in Eqn. (11)) for each segment, memory needs are reduced substantially compared with FEA requirements. For the cases considered in Fig. 6, the volume analyzed can be increased by over an order of magnitude and the memory requirement of the electrochemical fin approach does not surpass the memory needed for the smallest FEA test case. For the  $200 \times 200 \times 200$  voxel ( $8 \times 10^6$  voxels) dataset, the electrochemical fin approach consumes  $\sim 15\%$  of the memory required for the finite element simulation. Beyond  $8 \times 10^6$  voxels,

**Table 2**

Computation times (solution step only) for finite element calculation and several electrochemical fin simulations of the SFM X-ray nanotomography microstructural data.

RVE size <sup>a</sup> (voxels)	Network size <sup>b</sup> (# of particles)	Computation time (s)	
		Electrochemical fin	FEA
1.10E+06	43	0.10	87
8.00E+06 <sup>c</sup>	515	0.41	754
8.00E+06 <sup>c</sup>	613	0.47	782
1.56E+07	1185	1.02	— <sup>d</sup>
2.04E+07	1384	1.30	— <sup>d</sup>
2.54E+07	1752	1.85	— <sup>d</sup>
3.05E+07	2046	2.30	— <sup>d</sup>
3.56E+07	2480	3.36	— <sup>d</sup>
4.58E+07	3285	5.69	— <sup>d</sup>

<sup>a</sup> RVE size defines the size of the digitized microstructural region extracted from the nanotomography dataset.

<sup>b</sup> Network size indicates the number of segments in the electrochemical fin network that are generated using the skeletonization routine after the sub-partitioning step.

<sup>c</sup> Computations performed on two RVEs of a same size.

<sup>d</sup> Finite element cases for larger volumes were not performed due to memory limitations encountered in mesh generation.

FEA could not be performed due to lack of memory. However, electrochemical fin analysis was readily performed up to the largest volume sizes available by X-ray nanotomography, with an incremental increase in memory requirement across the range of RVE sizes considered. Memory requirements for the electrochemical fin method appear to scale about linearly with computational domain volume, compared to non-linear memory scaling for FEA and LBM methods. This reduced memory need allows for rapid assessment of microstructures on the scale of active regions on a personal computer, and the analysis of large regions becomes much more feasible. Furthermore, the dramatic improvement in solution speed permits execution of numerous studies and optimization of real structures and large scale deterministic structures. In summary, the electrochemical fin approach demonstrates a computational solution time requirement that is three orders of magnitude faster than the finite element model and around six orders of magnitude faster than LBM for the same microstructural region. As a final consideration, we note that lattice Boltzmann simulations for charge transport were initiated as a means of comparing to the electrochemical fin approach. However, these investigations were terminated in favor of using FEA models. In the absence of surface charge transfer, LBM simulations of the small test region using previously developed codes [8,40] required on the order of one week to complete with sufficient accuracy. An LBM simulation that is comparable to the current electrochemical fin study will need to include surface charge transfer due to electrochemical reactions at the surface. Such an LBM case is estimated to require several weeks to complete.

The computational savings gained by the basic network model are rooted in the scaling behavior of each approach. Closer inspection of these computational cost comparisons reveals that performance of the electrochemical fin model is tied more to the number of particles in the network than to the total volume of the structure. The related computational requirements are therefore expected to scale primarily with the geometric complexity of the structure. This stands in contrast with mesh-based and grid-based methods, for which degrees of freedom and computational requirements can be expected to scale with both geometric complexity and system volume. Considering a larger volume comparable to the SFM structures considered in the present work, meshed at close to single voxel accuracy, moving from a cubic RVE with sides of length  $5\text{ }\mu\text{m}$  ( $8 \times 10^6$  voxels) to a cubic RVE with side lengths of  $10\text{ }\mu\text{m}$  could increase memory requirements from  $\sim 6\text{ GB}$  to  $\sim 45\text{ GB}$ . This estimate assumes around 1.4 DOF per element and similar memory needs (bytes per DOF) as seen in smaller scale studies. Moving to representative volume sizes indicative of non-support electrodes, i.e. on the order of  $20\text{--}50\text{ }\mu\text{m}$  per side, could easily drive memory requirements to terabyte scales in mesh-based approaches, without the addition of more complex physics.

Considering these advantages, it is important to note the limitations of electrochemical fin theory. Specifically, this approach does not account for transport of multiple charged species, and it does not address mass transport within the pore phase. The first of these limitations is rooted in the assumptions that permit development of the analytical electrochemical fin model and relegate the approach to primarily a screening tool that complements more rigorous microstructural design efforts. In addressing transport of a single charged species, the coupling between ionic and electronic transport is not accounted for in the current version of the model. For materials in which transport is largely controlled by one carrier, such as the SFM herein addressed, this focused assessment is considered sufficient. However, as seen in the polarization resistance predictions above, this simplification leads to a loss of accuracy. It should be noted that accounting for mixed conduction would require numerical solution at a substantially higher cost due

to increased DOFs associated with inclusion of electronic transport and vacancy incorporation mechanisms. Further cost would be entailed by including gas transport using either Stefan–Maxwell or dusty-gas formalisms. Based on requirements seen in cell-level mixed conduction analyses, the number of degrees of freedom solved for in such a problem could be multiplied by approximately 2–5 times the value seen for single carrier transport simulations. This substantial increase in cost would likely preclude multi-physics simulations on the largest scales that can be achieved with the electrochemical fin theory. Even when feasible, these costs warrant the use of the rapid first stage assessment and screening capabilities provided by the electrochemical fin approach.

In addition to considering single carrier transport, the electrochemical fin theory does not account for space charge effects that may occur between individual particles. This effect may be added through the incorporation of nodal resistances within the network. Such measures were not considered in the current work for two reasons. First, the X-ray nanotomography technique applied does not provide data that distinguishes grain boundaries, so the microstructure cannot currently be separated based on true grain boundaries. Second, addition of space charge effects within the structure has been shown to have little effect on the screening capabilities of the electrochemical fin model [7], so the approximation is considered sufficient.

Geometric limitations are also present in the model. As noted, the methodology outlined approximates transport through irregularly shaped particles in the microstructure using an analytical model based on a smoothed shape with an exponentially varying cross-sectional area. This approximation is based on the application of an average sintering quality for each network segment that is calculated using Eqn. (13). Through this approximation, details of the microstructure below the level of the individual segment are homogenized. Hence the technique may not fully account for constrictions within an individual segment that can increase conductive transport resistance. This limitation can be mitigated by modifying partitioning methods to monitor local variations in curvature and use these variations to define vertices between segments. Such sub-partitioning proves challenging for irregular segment shapes and may lead to ambiguities when partitioning a structure. In the present studies, sub-partitioning was limited to one constriction per skeleton edge. As an alternative, it may prove feasible to use dimensionless parameters to inform selection of well-defined shapes, e.g. conical or spherical segments, to simulate parts of the microstructure. Finally, certain microstructural morphologies may also present challenges to implementing the electrochemical fin approach. Knotted regions, where more than two or three segments connect at a vertex, and highly tortuous segments may not be captured as well as detailed mesh-based methods may permit. Due diligence must be exacted during segmentation, skeletonization, and parameter estimation to ensure segments are representative of their respective microstructural regions.

The ability of the skeleton-based partitioning to provide a meaningful representation of a material has been evaluated for X-ray nanotomography measurements of Ni-YSZ and LSM-YSZ composite SOFC electrodes [43]. For partitioned structures intra- and inter-phase coordination numbers and discrete phase size distributions can be computed based on the skeleton information and the equivalent spherical radius of each particle, respectively. Coordination number measurements based on the partitioned volume are comparable to predictions from percolation theory. Phase size distributions obtained from discrete particle sizes and those based on morphological operations on a non-partitioned volume also show agreement. Both percolation theory and morphological operations are commonly applied to SOFC composite electrodes produced by conventional methods [44,45]. For the  $5\text{ }\mu\text{m}$  SFM RVEs,



adjustments of the partitioning parameters described in Section 2.1 modify the computed polarization resistance by 12% at most. Inaccuracies in the measurement of the surface areas can cause larger discrepancies. The applied marching cube algorithm significantly alleviates overestimation compared to voxel face counting, yet is known to overestimate the surface area of a sphere by 8% [13]. Calculation of the sintering quality and resistivity ratio from smoothed surfaces resulted in computed polarization resistances up to 22% higher. Such a range of uncertainties is considered acceptable for a screening tool, for which sensitivity to microstructural effects rather than absolute accuracy is crucial. However, this uncertainty underscores the importance of properly characterizing the cross-sectional and surface areas that define the sintering quality and resistivity ratio.

As noted above, the edge-based partitioning step is considered comparable to the demands of generating a quality mesh for finite element or finite volume studies of complex structures. Hence, the performance comparisons shown in Fig. 6 and Table 2 are provided for the solution step only. Preliminary studies suggest that the number of network segments that can be extracted from a microstructural dataset is primarily restricted by software memory limitations. With the above caveats in mind, the electrochemical fin approach provides a powerful tool for the design and optimization of both deterministic and real microstructures.

## 5. Conclusions

The analytical electrochemical fin theory has been adapted for the analysis of real SOFC electrode microstructures. The basis for this adaptation lies in applying the non-dimensional form of the electrochemical fin model to microstructural networks partitioned from data obtained using three-dimensional imaging techniques. Using data from X-ray nanotomography measurements of porous, mixed-conducting electrodes composed of  $\text{Sr}_2\text{Fe}_{1.5}\text{Mo}_{0.5}\text{O}_{6-\delta}$ , a methodology for network partitioning has been developed and demonstrated herein. Estimation of electrochemical fin model parameters from individual segments within this microstructural network permits rapid analysis of transport within real microstructures while retaining effects of localized morphology. In addition to accounting for these effects, the approach developed incorporates the influence of network topology on charge transport.

Performance estimates based on the analysis of electrochemical fin networks extracted from the SFM image data are compared to estimates made using three-dimensional finite element models. While the distinct levels of detail exist for each of these approaches, the streamlined electrochemical fin theory proves capable of predicting behavior within reasonable error compared to the finite element predictions. The greatest discrepancy observed for these approaches relates to fin network vertices that are in close proximity to, but not located expressly on, RVE boundaries. In this case, transport distances within the network serve as an overestimate of true transport distances. While the details of transport show some discrepancy, predictions of electrode polarization resistances made with each approach agree well. This suggests that estimation of such performance metrics using the electrochemical fin theory is sufficient for assessment of real electrode microstructures. Polarization resistances estimated for larger RVEs taken from the X-ray nanotomography data underestimate resistance when compared to experimental measurements for SFM. However, these estimates are of comparable magnitude and some discrepancy is expected due to simplifying assumptions applied in development of the analytical model. Most notably, the approach presented focuses on single carrier transport for the limiting species, oxygen anions in SFM.

Clear benefits of implementing the electrochemical fin theory are seen when comparing computational requirements to those of

FEA models. For the electrochemical fin network model, memory requirements are significantly less than FEA and LBM methods, giving it the potential to investigate large structures that are currently intractable using FEA and LBM methods. Even for the analysis of single carrier transport the memory needs for the latter numerical techniques can rapidly scale due to the volumetric dependence of degrees of freedom solved. For representative volumes on the order of 50  $\mu\text{m}$  per side, these requirements can approach the terabyte scale and can be expected to multiply further as more advanced multiphysics simulation of mixed conduction and gas transport increase the number of variables analyzed. In contrast, memory requirements for the electrochemical fin network approach scale at a slower rate due to its dependence on network complexity. Savings with respect to computational time requirements are substantially greater than those seen for memory requirements. Solution times for the electrochemical fin approach are approximately three orders of magnitude lower than those required for FEA models, and six orders of magnitude lower than those required for LBM. These less stringent memory and computational time requirements allow electrochemical fin theory to be used as a rapid, yet sufficiently detailed, microstructure performance assessment tool on a personal computing platform. These enhanced computational capabilities reinforce the relevance of the electrochemical fin theory as a tool for rapidly assessing and optimizing future SOFC electrode designs and designs of other electrochemical energy storage and conversion devices.

## Acknowledgments

Financial support from an Energy Frontier Research Center on Science Based Nano-Structure Design and Synthesis of Heterogeneous Functional Materials for Energy Systems (HeteroFoam Center) funded by the U.S. Department of Energy, Office of Science, Office of Basic Energy Sciences (Award DE-SC0001061) is gratefully acknowledged. Portions of this research were carried out at the Advanced Photon Source supported by the U.S. Department of Energy, Office of Science, Office of Basic Energy Sciences, under contract No. DE-AC02-06CH11357. The authors thank W. M. Harris for comments provided on image processing and analysis.

## References

- [1] K. Reifsnider, X. Huang, G. Ju, R. Solasi, *Journal of Materials Science* 41 (2006) 6751.
- [2] W.K.S. Chiu, A.V. Virkar, F. Zhao, K.L. Reifsnider, G.J. Nelson, F. Rabbii, Q. Liu, *Journal of Fuel Cell Science and Technology* 9 (2012).
- [3] F. Zhao, A.V. Virkar, *Journal of Power Sources* 195 (2010) 6268.
- [4] S.W. Sofie, *Journal of the American Ceramic Society* 90 (2007) 2024.
- [5] Q. Liu, X. Dong, C. Yang, S. Ma, F. Chen, *Journal of Power Sources* 195 (2010) 1543.
- [6] G.J. Nelson, A.A. Peracchio, W.K.S. Chiu, *Journal of Power Sources* 196 (2011) 4695.
- [7] G.J. Nelson, B.N. Cassenti, A.A. Peracchio, W.K.S. Chiu, *Journal of Power Sources* 205 (2012) 48.
- [8] K.N. Grew, Y.S. Chu, J. Yi, A.A. Peracchio, J.R. Izzo, Y. Hwu, F.D. Carlo, W.K.S. Chiu, *Journal of the Electrochemical Society* 157 (2010) B783.
- [9] J.R. Wilson, W. Kobsiriphat, R. Mendoza, H.Y. Chen, J.M. Hiller, D.J. Miller, K. Thornton, P.W. Voorhees, S.B. Adler, S.A. Barnett, *Nature Materials* 5 (2006) 541.
- [10] J.R. Wilson, A.T. Duong, M. Gameiro, H.Y. Chen, K. Thornton, D.R. Mumm, S.A. Barnett, *Electrochemistry Communications* 11 (2009) 1052.
- [11] G.J. Nelson, W.M. Harris, J.R. Izzo, K.N. Grew, W.K.S. Chiu, Y.S. Chu, J. Yi, J.C. Andrews, Y. Liu, P. Pianetta, *Applied Physics Letters* 98 (2011) 173109.
- [12] N. Shikazono, D. Kanno, K. Matsuzaki, H. Teshima, S. Sumino, N. Kasagi, *Journal of the Electrochemical Society* 157 (2010) B665.
- [13] K. Matsuzaki, N. Shikazono, N. Kasagi, *Journal of Power Sources* 196 (2011) 3073.
- [14] J. Laurencin, R. Quey, G. Delette, H. Suhonen, P. Cloetens, P. Bleuett, *Journal of Power Sources* 198 (2012) 182.
- [15] P. Costamagna, P. Costa, V. Antonucci, *Electrochimica Acta* 43 (1998) 375.
- [16] M. Cannarozzo, S. Grosso, G. Agnew, A.D. Borghi, P. Costamagna, *Journal of Fuel Cell Science and Technology* 4 (2007) 99.
- [17] H. Zhu, R.J. Kee, *Journal of the Electrochemical Society* 155 (2008) B715.
- [18] J.H. Nam, D.H. Jeon, *Electrochimica Acta* 51 (2006) 3446.



- [19] P. Tanasini, M. Cannarozzo, P. Costamagna, A. Faes, J. Van herle, A. Hessler-Wyser, C. Comninellis, *Fuel Cells* 9 (2009) 740.
- [20] L.C.R. Schneider, C.L. Martin, Y. Bultel, D. Bouvard, E. Siebert, *Electrochimica Acta* 52 (2006) 314.
- [21] L.C.R. Schneider, C.L. Martin, Y. Bultel, L. Dessemond, D. Bouvard, *Electrochimica Acta* 52 (2007) 3190.
- [22] S. Sunde, *Journal of Electroceramics* 5 (2000) 153.
- [23] S. Sunde, *Journal of the Electrochemical Society* 143 (1996) 1123.
- [24] S. Sunde, *Journal of the Electrochemical Society* 143 (1996) 1930.
- [25] T. Kenjo, S. Osawa, K. Fujikawa, *Journal of the Electrochemical Society* 138 (1991) 349.
- [26] T. Kenjo, M. Nishiya, *Solid State Ionics* 57 (1992) 295.
- [27] C.W. Tanner, K.-Z. Fung, A.V. Virkar, *Journal of the Electrochemical Society* 144 (1997) 21.
- [28] G. Xiao, Q. Liu, F. Zhao, L. Zhang, C. Xia, F. Chen, *Journal of the Electrochemical Society* 158 (2011) B455.
- [29] G. Xiao, Q. Liu, S. Wang, V.G. Komvokis, M.D. Amiridis, A. Heyden, S. Ma, F. Chen, *Journal of Power Sources* 202 (2012) 63.
- [30] X. Guo, J. Maier, *Journal of the Electrochemical Society* 148 (2001) E121.
- [31] Q. Liu, X. Dong, G. Xiao, F. Zhao, F. Chen, *Advanced Materials* 22 (2010) 5478.
- [32] G.J. Nelson, W.M. Harris, J.J. Lombardo, J.R. Izzo, W.K.S. Chiu, P. Tanasini, M. Cantoni, J. Van herle, C. Comninellis, J.C. Andrews, Y. Liu, P. Pianetta, Y.S. Chu, *Electrochemistry Communications* 13 (2011) 586.
- [33] G.J. Nelson, K.N. Grew, J.R. Izzo, J.J. Lombardo, W.M. Harris, A. Faes, A. Hessler-Wyser, J.V. Herle, S. Wang, Y.S. Chu, A.V. Virkar, W.K.S. Chiu, *Acta Materialia* 60 (2012) 3491.
- [34] W.S. Rasband, *ImageJ*, n.d.
- [35] M. Sato, I. Bitter, M.A. Bender, A.E. Kaufman, M. Nakajima, in: *Proceedings of the Eighth Pacific Conference on Computer Graphics and Applications*, 2000, p. 281.
- [36] M.E. Lynch, D. Ding, W.M. Harris, J.J. Lombardo, G.J. Nelson, W.K.S. Chiu, M. Liu, *Nano Energy* (2012).
- [37] Q. Fang, D.A. Boas, in: *2009 IEEE International Symposium on Biomedical Imaging: from Nano to Macro, ISBI 2009*, 2009, pp. 1142–1145.
- [38] A. Okabe, B. Boots, K. Sugihara, D.S.N. Chiu, *Spatial Tessellations: Concepts and Applications of Voronoi Diagrams*, John Wiley & Sons, 2009.
- [39] K.N. Grew, A.A. Peracchio, A.S. Joshi, J.R. I. Jr., W.K.S. Chiu, *Journal of Power Sources* 195 (2010) 7930.
- [40] K.N. Grew, A.A. Peracchio, W.K.S. Chiu, *Journal of Power Sources* 195 (2010) 7943.
- [41] J.R. Wilson, J.S. Cronin, A.T. Duong, S. Rukes, H.-Y. Chen, K. Thornton, D.R. Mumm, S. Barnett, *Journal of Power Sources* 195 (2010) 1829.
- [42] J.R. Wilson, J.S. Cronin, S.A. Barnett, *Scripta Materialia* 65 (2011) 67.
- [43] A. Nakajo, G.J. Nelson, M.B. DeGostin, T.D. Myles, A.A. Peracchio, W.K.S. Chiu, in: *Proceedings of IMECE2012, ASME, Houston, TX, United States, 2012*, Paper No. IMECE2012-86133.
- [44] D. Chen, Z. Lin, H. Zhu, R.J. Kee, *Journal of Power Sources* 191 (2009) 240.
- [45] L. Holzer, B. Iwanschitz, T. Hocker, B. Münch, M. Prestat, D. Wiedenmann, U. Vogt, P. Holtappels, J. Sfeir, A. Mai, T. Graule, *Journal of Power Sources* 196 (2011) 1279.